

Impulse propagation over a complex site: A comparison of experimental results and numerical predictions

Didier Dagna^{a)} and Philippe Blanc-Benon

Laboratoire de Mécanique des Fluides et d'Acoustique, UMR CNRS 5509, École Centrale de Lyon, Université de Lyon, 36 Avenue Guy de Collongue, 69134 Écully Cedex, France

Franck Poisson

Société Nationale des Chemins de fer Français, 40 Avenue des Terroirs de France, 75611 Paris Cedex 12, France

(Received 23 May 2013; revised 13 January 2014; accepted 16 January 2014)

Results from outdoor acoustic measurements performed in a railway site near Reims in France in May 2010 are compared to those obtained from a finite-difference time-domain solver of the linearized Euler equations. During the experiments, the ground profile and the different ground surface impedances were determined. Meteorological measurements were also performed to deduce mean vertical profiles of wind and temperature. An alarm pistol was used as a source of impulse signals and three microphones were located along a propagation path. The various measured parameters are introduced as input data into the numerical solver. In the frequency domain, the numerical results are in good accordance with the measurements up to a frequency of 2 kHz. In the time domain, except a time shift, the predicted waveforms match the measured waveforms with a close agreement.

© 2014 Acoustical Society of America. [<http://dx.doi.org/10.1121/1.4864286>]

PACS number(s): 43.28.Gq, 43.28.Js, 43.28.En, 43.20.El [VEO]

Pages: 1096–1105

I. INTRODUCTION

Outdoor sound propagation problems are in most of the cases complex, because they involve multiphysics phenomena linked to the inhomogeneities of the atmosphere or to the interaction of acoustic waves with the ground. Thus, numerical simulations are necessary to accurately predict acoustic propagation above a realistic site. In particular, time-domain approaches are an active field of research. Many recent studies were concerned with the introduction of numerical methods (Salomons *et al.*, 2002; Ostashev *et al.*, 2005; Hornikx *et al.*, 2010), modeling of ground effects (Wilson *et al.*, 2007; Cotté *et al.*, 2009; Guillaume *et al.*, 2011), and direct applications (Van Renterghem and Botteldooren, 2003; Heimann, 2010). Among them, a finite-difference time-domain solver was proposed to treat outdoor sound propagation in a complex environment by the present authors (Dagna *et al.*, 2013). In this work, curvilinear coordinates were employed to deal with non-flat terrain. The time-domain impedance boundary condition proposed by Cotté *et al.* (2009) was implemented at the ground to account for reflection over impedance surfaces. This solver was validated against test cases dealing with diffraction by cylindrical or spherical impedance surfaces.

In the present paper, results obtained with the time-domain numerical solver are compared to experimental data in both the frequency domain and time domain. The main objective is to show that time-domain approaches allow one to consider realistic outdoor sound propagation problems

with complex meteorological conditions and ground surfaces. The outdoor acoustic measurements were carried out in La Veuve, France in May 2010 on a railway site. The impulse signals of the acoustic pressure generated using pistol shots were recorded at three microphones along a line. This line determines the sound propagation path along which the sound field has been studied. The ground characteristics, which are the topography and the ground surface impedances, and the meteorological conditions were determined *in situ*. This study is related to previous research done on the propagation of impulse signals in the atmosphere by Cramond and Don (1985) and by Albert and Orcutt (1989).

The paper is organized as follows. In Sec. II, the experimental site is described. Measurements of the ground profile, the acoustic characteristics of the ground, and the meteorological conditions are reported. The values of the deduced parameters are discussed, especially for the ballast surface. In Sec. III, the numerical solver is presented. Comparisons of the acoustic pressure determined from the experiments and from the numerical simulations are shown at three receivers in both frequency and time domains. The influence of the wind direction on the results is then investigated.

II. DESCRIPTION OF THE EXPERIMENTAL SITE

The experimental campaign was carried out on a railway site with a ballasted track in La Veuve near Reims in France in May 2010 by the Société Nationale des Chemins de fer Français (SNCF) test department. The sound propagation path (along which the sound field is studied) is perpendicular to the railway track (see Fig. 1). The origin of the Cartesian coordinates system is located in the middle of the track, on the top of the rail and on the propagation path. The x axis

^{a)}Author to whom correspondence should be addressed. Electronic mail: didier.dagna@ec-lyon.fr

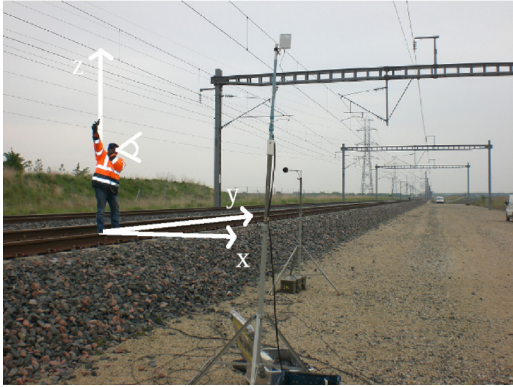


FIG. 1. (Color online) Position of the acoustic source (alarm pistol) on the experimental site.

coincides with the propagation path, the y axis is parallel to the railway track, and the z axis is vertical. A photograph depicted in Fig. 2, taken from the top of the ballast bed, shows the propagation path considered in this study.

Along the propagation path, three type 4188 1/2-in. Brüel & Kjær microphones were positioned at different distances, as shown in Fig. 3. Thereafter, they are denoted by M_1 , M_2 , and M_3 and are located, respectively, at $(x = 7.5 \text{ m}, y = 0 \text{ m}, z = 1.2 \text{ m})$, $(x = 25 \text{ m}, y = 0 \text{ m}, z = 3.5 \text{ m})$, and $(x = 100 \text{ m}, y = 0 \text{ m}, z = 1.85 \text{ m})$.

A. Topography and ground surface impedances

The topography of the site was measured along the propagation path. The ground profile is shown as a function of the distance in Fig. 3. It is relatively flat except for the ballast bed and near the gap between the soil and the grass around $x = 20 \text{ m}$. The depth of the gap is close to 0.8 m .

Five ground types, which are a ballast bed, a soil, a grassy ground, a road, and a field, were distinguished along the propagation path. They are represented with different colors in Fig. 3. The road is modeled by a rigid ground, corresponding to an infinite surface impedance. In order to get a surface impedance model for the other types of ground, *in situ* measurements using the transfer function method [as described, e.g., in ANSI/ASA S1.18-2010 (2010)] were performed by l'Institut Français des Sciences et Technologies des Transports, de l'Aménagement et des Réseaux



FIG. 2. (Color online) Photograph of the experimental site showing the propagation path.

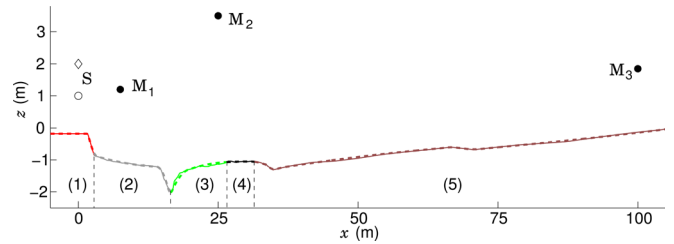


FIG. 3. (Color online) Topography of the experimental site obtained from the measurements (solid line) and implemented in the numerical solver (dashed line). The colors and numbers correspond to the different types of ground: (1) ballast, (2) soil, (3) grassy ground, (4) road, and (5) field. Position of the source (S) for $z_S = 1 \text{ m}$ (white circle) and for $z_S = 2 \text{ m}$ (diamond) and of the receivers M_1 , M_2 , and M_3 (black circle).

(IFSTTAR). The method is to put an omnidirectional source and two microphones above the ground, as depicted in Fig. 4, and to compute the transfer function T , which is the ratio of the Fourier transforms of the acoustic pressure at the two microphones. The transfer function is also computed using an analytical solution. As the geometry is known, the analytical expression of T is only a function of the surface impedance. The parameters of a given surface impedance model can thus be determined to have the best agreement between the transfer function determined from the experimental results and from the analytical solution.

Surface impedance models are sought in the form of a rigidly backed layer of thickness d_L :

$$Z_L = Z_c \coth(-ik_c d_L), \quad (1)$$

where Z_c and k_c are, respectively, the characteristic impedance of the soil and the wavenumber in the layer. This surface impedance model aims at representing a layer of porous medium above a rigid surface. It is classically used in outdoor sound propagation studies (Rasmussen, 1985; Cotté *et al.*, 2009; Attenborough *et al.*, 2011) as an alternative of the semi-infinite ground model and can allow one to obtain a better agreement between the transfer function determined experimentally and analytically in some cases (Attenborough *et al.*, 2011). As noted by Attenborough *et al.* (2011), it is generally difficult to deduce more than two impedance model parameters by using the transfer function method. Therefore, the Miki one-parameter impedance model (Miki, 1990)

$$Z_c = \rho_0 c_0 \left[1 + \mu \left(\frac{\sigma_0}{-i\omega\rho_0} \right)^b \right], \quad (2)$$



FIG. 4. (Color online) Sketch of the measurement set-up for the transfer function method.

$$k_c = k \left[1 + \nu \left(\frac{\sigma_0}{-i\omega\rho_0} \right)^q \right], \quad (3)$$

where σ_0 is the effective air flow resistivity and ρ_0 the air density, is used to characterize the soil, the grassy ground, and the field. The reference sound speed c_0 is the value of the sound speed c at the ground. The angular frequency and the acoustic wavenumber are denoted, respectively, by ω and $k = \omega/c_0$. The numerical parameters of the Miki impedance models are $\mu = 0.459$, $\nu = 0.673$, $b = 0.632$, and $q = 0.618$. The moduli of the transfer functions are represented as a function of the frequency for the different grounds in Fig. 5. It is observed that good fits are obtained for these ground types using the Miki one-parameter impedance model. Other one- or two-parameter impedance models proposed in the literature, such as the two-parameter slit-pore model (Attenborough *et al.*, 2011), can also lead to accurate fits. The deduced values of the impedance model parameters are given for the different grounds in Table I. Parameters obtained for the field and the grassy ground are similar, because as observed in Fig. 5 the corresponding transfer functions are very close.

For the ballast bed, it was not possible to obtain an acceptable fit from the measurements done in La Veuve site. Indeed, it was complicated to account for the thickness effect, as the thickness of the ballast bed is not constant across its width, and to overcome the multiple reflections on the rails and on the soil. Additional measurements were performed on IFSTTAR's site in Bouguenais, France. To do so, a 25 cm thick layer of ballast with porosity $\Omega = 0.5$ was put on an asphalt ground. Then, the transfer function method has been applied to determine the characteristics of the ballast surface. In the fitting procedure, the thickness of the ballast bed and its porosity are chosen as the actual ones, which are $d_L = 25$ cm and $\Omega = 0.5$. As shown in Fig. 5(a), a good fit is obtained by using the Hamet and Bérengier impedance model (Bérengier *et al.*, 1997)

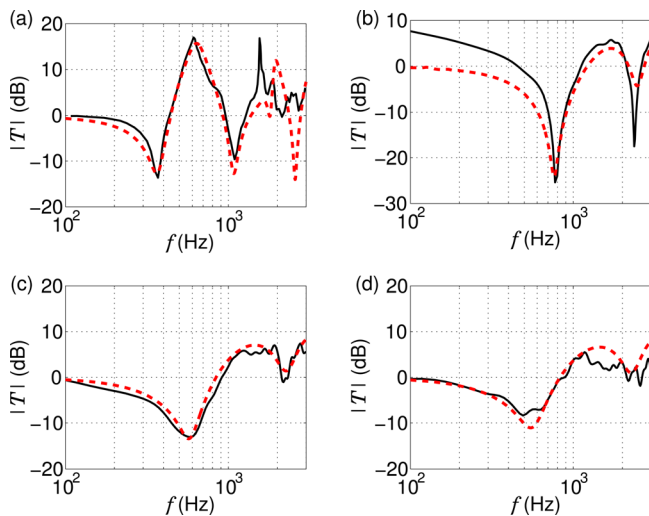


FIG. 5. (Color online) Transfer function T determined experimentally (solid line) and calculated analytically with best fit (dashed line) (a) for the ballast, (b) for the soil, (c) for the grassy ground, and (d) for the field.

TABLE I. Effective parameters of the surface impedance models.

	Miki			Hamet and Bérengier
	Soil	Grassy ground	Field	Ballast bed
σ_0 , kPa s m ⁻²	600	180	170	0.3
d_L , m	0.006	0.018	0.022	∞
q	—	—	—	1.12
Ω	—	—	—	0.5

$$Z_c = \frac{\rho_0 c_0 q}{\Omega} \left[1 + \frac{\omega_1}{-i\omega} \right]^{1/2} \left[1 + \frac{\omega_2}{-i\omega} \right]^{1/2} \left[1 + \frac{\omega_3}{-i\omega} \right]^{-1/2}, \quad (4)$$

$$k_c = kq \left[1 + \frac{\omega_1}{-i\omega} \right]^{1/2} \left[1 + \frac{\omega_2}{-i\omega} \right]^{-1/2} \left[1 + \frac{\omega_3}{-i\omega} \right]^{1/2}, \quad (5)$$

where the different parameters are given by

$$\omega_1 = \frac{\sigma_0 \Omega}{\rho_0 q^2}, \quad \omega_2 = \frac{\sigma_0}{\rho_0 N_{Pr}}, \quad \text{and} \quad \omega_3 = \frac{\gamma \sigma_0}{\rho_0 N_{Pr}}. \quad (6)$$

In the above equations, q , Ω , N_{Pr} , and γ denote, respectively, the tortuosity, porosity, Prandtl number, and ratio of specific heats.

In the literature, other impedance models are proposed to characterize ballast surfaces. Heutschi (2009) has developed a model based on an electrical network analysis, which is closely related to the Zwicker and Kosten model described, for instance, in Salomons (2001). Air viscosity and geometrical parameters of the ballast stones are used as input parameters. Heutschi has performed experiments and comparisons with this model and with a four-parameter impedance model proposed by Attenborough (1985), which corresponds to a low frequency and/or high flow resistivity approximation of the cylindrical-pore model. Interestingly, analytical expressions of the Attenborough's four-parameter model are close to those of the Hamet and Bérengier impedance model. Recently, others comparisons with measurements have been provided by Attenborough *et al.* (2011) using a slit-pore model. Both studies show that one-parameter impedance models are not sufficient to characterize ballast surfaces. Accounting for extended reaction allows us to improve the comparisons.

The impedance model parameters obtained for the ballast bed in Bouguenais are given in Table I. The porosity and the effective tortuosity are in the same order of magnitude than values given in Heutschi (2009) and Attenborough *et al.* (2011). The effective flow resistivity is very small, which is also retrieved in the results provided in Attenborough *et al.* (2011).

B. Source

The acoustic source was a 0.9 caliber alarm pistol (see Fig. 1). The source was set to four heights, but here we will consider only heights of $z_S = 1$ m and of $z_S = 2$ m. The experiments were carried out on an operating site, which is representative of propagation conditions for applications in

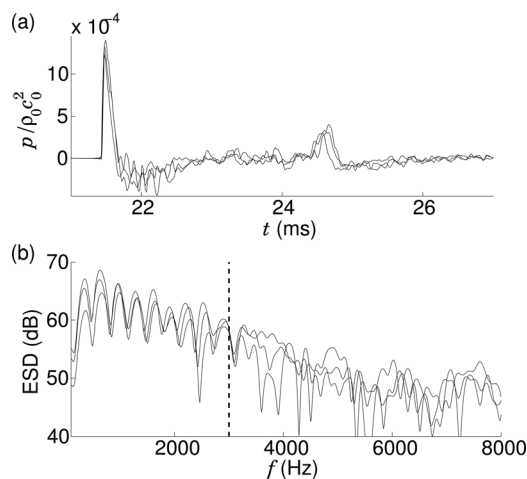


FIG. 6. (a) Waveforms as a function of the time and (b) corresponding ESDs of the acoustic pressure as a function of the frequency obtained at the receiver M_1 (at $x=7.5$ m) for the three shots fired for a source height $z_S = 1$ m. The reference for the dB calculation is $4 \times 10^{-10} \text{ Pa}^2 \text{ s}^2$. The vertical dashed line corresponds to the limit $f = 3$ kHz.

railway transportation noise on a ballasted track. However, it was not possible to install a positioning system on the track to accurately determine the location of the source. A positioning error on the order of the decimeter is thus expected. Three shots were fired for each source height. The waveforms of the acoustic pressure $p(t)$ obtained at the receiver M_1 at $x=7.5$ m for a source height $z_S = 1$ m are plotted in Fig. 6(a) as a function of the time. Note that they are very similar, as two arrivals related to the direct and to the reflected waves are clearly distinguished for each shot. The arrival times are also in close agreement. The corresponding energy spectral densities (ESDs) $|\hat{p}|^2$, where \hat{p} is the Fourier transform of the acoustic pressure, are computed from the waveforms and are represented as a function of the frequency in Fig. 6(b). Throughout the paper, the notation \hat{f} refers to the Fourier transform of the quantity f . A large variability is observed for the energy spectral densities for frequencies above approximately 3 kHz. In particular, the position of the interferences strongly depends on the pistol shot. Because the error on the position of the source is estimated at 0.1 m, comparisons with the measurements will be only shown for frequencies below 3 kHz, which corresponds to a wavelength of 0.1 m.

The source is assumed to be monopolar, as its directivity was not measured. The source strength of the experimental source, denoted by $S_{\text{exp}}(\omega)$, is then computed from the waveforms. For that, the waveform at the receiver M_1 at $x=7.5$ m is considered, and the waveform of the direct wave, denoted by $p_D(t)$, is obtained by windowing the signal. Figure 7 shows an example of the part of a waveform associated to the direct wave. The Fourier transform of the direct wave can be expressed as the product of the 3-D Green's function in the free field and the source strength $S_{\text{exp}}(\omega)$

$$\hat{p}_D(\omega) = -S_{\text{exp}}(\omega) \frac{\exp(ik_{\text{eff}}R)}{4\pi R}, \quad (7)$$

where R is the distance between the source and the receiver and with $k_{\text{eff}} = \omega/c_{\text{eff}}$. The term c_{eff} corresponds to the

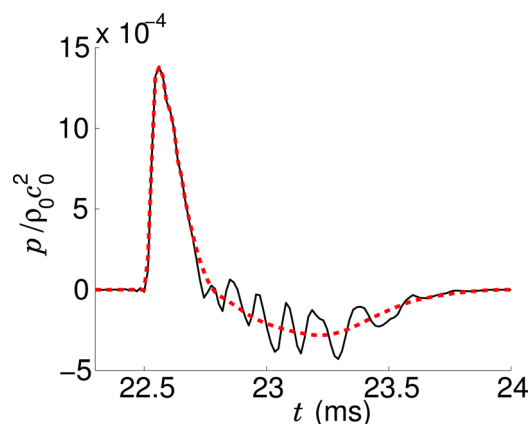


FIG. 7. (Color online) Part of the waveform corresponding to the direct wave obtained at the receiver M_1 (at $x=7.5$ m) for a given shot pistol as a function of the time: measured waveform (solid line) and its approximation (dashed line).

effective sound speed. The source strength, corresponding to the waveform represented in Fig. 7, is plotted as a function of the frequency in Fig. 8. It acts as a band-pass filter. The maximum of $|S_{\text{exp}}|$ is obtained at a frequency close to 900 Hz. It can also be noted that the frequency content of the source pulse goes up to 10 kHz approximately.

High-frequency oscillations are observed on the waveforms during the expansion phase. They are mainly due to the resonance of the microphones. An approximation of the waveforms by quadratic splines is used to get rid of these oscillations (see Fig. 7). The corresponding source strength is plotted as a function of the frequency in Fig. 8. It is seen that the low frequency part is the same than that deduced from the measured waveform. Only the frequency content above 3 kHz is modified by the approximation.

C. Meteorological conditions

A meteorological mast was installed on the site at $x = 125$ m near the propagation path along which the sound field is studied. Three Young 05103-5 propeller anemometers and three Vectors Instruments T302 temperature sensors were set at heights of 1, 3, and 10 m. A MP103A-CG030-W4W Rotronic humidity sensor was also installed at a height of 3 m. A Vaisala model PTB-101 barometer was used to

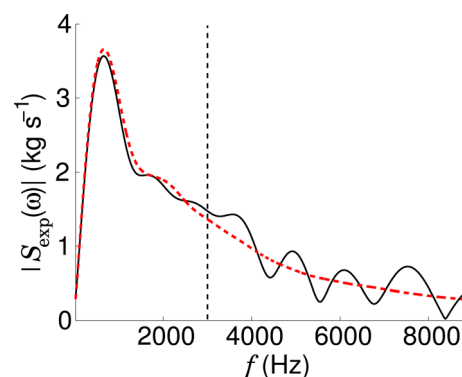


FIG. 8. (Color online) Source strength as a function of the frequency for the measured waveform (see Fig. 7) (solid line) and for its approximation (dashed line). The vertical dashed line corresponds to the limit $f = 3$ kHz.

TABLE II. Measured values of meteorological conditions.

z , m	P_0 , hPa	r_h , %	T_0 , °C	ρ_0 , kg m ⁻³	c , m s ⁻¹
1 m	991	82	6.1	1.24	—
3 m			6.4	1.24	—
10 m			6.7	1.24	335.5

determine the atmospheric pressure. At last, a Campbell Scientific CSAT3 sonic anemometer was located at a height of 10 m.

Table II gives the measured values of the atmospheric pressure P_0 , the relative humidity r_h , the temperature T_0 , the air density ρ_0 , and the sound speed c , which are nearly constant during the experimental campaign. The time variations of the wind speed V_0 and its direction relative to the propagation path θ are found to be more important. The values of V_0 and θ averaged over 1 min are used in this study and are given for both source heights in Table III.

The mean vertical profiles of wind V_0 and temperature T_0 are obtained from the Monin–Obukhov similarity theory, described, e.g., in Salomons (2001). Although this theory is not applicable for inhomogeneous non-flat grounds, it allows us to estimate realistic vertical profiles from a low number of measurements. A technique based on an optimization method (Cotté, 2008) is used to find the coefficients of the profiles. Figures 9(a) and 9(b) show, respectively, the mean vertical profiles of temperature and wind speed as a function of height above the ground. As said in the previous paragraph, the temperature profile is the same for both source heights. However, the wind velocity profile is different for the cases $z_S = 1$ m and $z_S = 2$ m. As the measurements were made during the morning, these profiles are characteristic of an unstable atmosphere.

The sound speed profile is calculated using the relation proposed by Cramer (1993), which account for the effects of the temperature, the humidity, the atmospheric pressure and the composition of the air on the sound speed. It is plotted as a function of the height above the ground in Fig. 9(c). Note that the value determined for c for a height of 10 m is very close to that measured by the sonic anemometer. In addition, the atmospheric absorption (Bass *et al.*, 1995) is neglected in this study, because the maximal value of the attenuation due to the atmospheric absorption is equal to -2 dB for the receiver M_3 at $x = 100$ m and for the frequency $f = 3$ kHz.

III. COMPARISON WITH NUMERICAL RESULTS

A. Numerical aspects

In this section, the measurements of acoustic pressure are compared to the results of a finite-difference time-domain

TABLE III. Measured values of wind velocity and direction.

z , m	V_0 , m s ⁻¹			θ , deg.		
	1 m	3 m	10 m	1 m	3 m	10 m
$z_S = 1$ m	3.3	3.5	4.0	297	304	315
$z_S = 2$ m	4.1	4.8	5.6	296	303	321

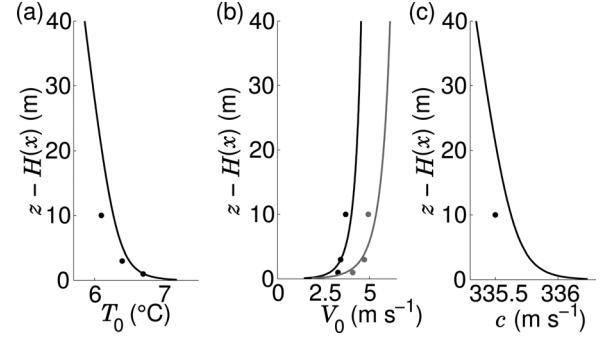


FIG. 9. Vertical profiles of (a) temperature, (b) wind speed and (c) sound speed as a function of the height above the ground. Measurements (circles) and determined profiles for $z_S = 1$ m (black solid line) and for $z_S = 2$ m (gray solid line).

(FDTD) solver. The linearized Euler equations with terms of order $(V_0/c)^2$ omitted (Ostashev *et al.*, 2005) are solved using high-order finite-difference techniques, developed in the computational aeroacoustics community (Bogey and Bailly, 2004). Curvilinear coordinates are used to account for the topography of the terrain. The time-domain impedance boundary condition proposed by Cotté *et al.* (2009) is implemented at the ground. At the outer boundaries, the radiation boundary condition proposed by Tam and Dong (1996) is implemented. Details on the solver and validation against test cases in 2-D and 3-D geometries are presented in Dragna *et al.* (2013). In a previous study, the solver was also used to examine long-range propagation of acoustic waves in a stratified atmosphere (Dragna *et al.*, 2011) over ground surfaces. Surface waves were exhibited.

Because the geometry of the railway track is invariant in the y -direction, the numerical simulation is performed in a 2-D configuration. The transformation from the curvilinear coordinates system to the Cartesian coordinate system is simply given by

$$x = \xi, \quad (8)$$

$$z = \eta + H(\xi), \quad (9)$$

where (ξ, η) are the curvilinear coordinates. Because of the use of curvilinear coordinates, the ground profile $H(x)$ has to be smooth, which means that it must be continuous and differentiable. The measured ground profile is thus approximated by quadratic splines, whose polynomial coefficients can be found in Dragna (2011). The ground profile implemented in the numerical solver is plotted in Fig. 3 in a dashed line as a function of the distance. It is observed that the discrepancies from the measured ground profile are small, typically less than one decimeter. In addition, a correction of the results of the numerical simulation has to be done to account for spherical spreading. Following Parakkal *et al.* (2010), the acoustic pressure \hat{p}^{3D} in a 3-D geometry (x, y, z) invariant in the y -direction is related to the acoustic pressure \hat{p}^{2D} in a 2-D geometry (x, z) by

$$\hat{p}^{3D}(x, y, z) = \hat{p}^{2D}(x, z) \sqrt{\frac{k_0}{2\pi i x}} \exp\left(\frac{i k_0 y^2}{2x}\right). \quad (10)$$

The acoustic source in the numerical simulations is a Gaussian impulse source. The simulation is thus initialized by setting

$$p(x, z, t = 0) = \rho_0 c_0^2 \exp\left(-\ln(2) \frac{x^2 + (z - z_S)^2}{B^2}\right), \quad (11)$$

$$\mathbf{v}(x, z, t = 0) = \mathbf{0}, \quad (12)$$

where the Gaussian halfwidth B has been set to 0.05 m. The source strength of the numerical source, denoted as $S_{\text{FDTD}}(\omega)$, is known analytically (Dragna *et al.*, 2011):

$$S_{\text{FDTD}}(\omega) = ik\pi B_x^2 \rho_0 c_0 \exp\left(-\frac{k^2 B_x^2}{4}\right), \quad (13)$$

with $B_x = B/\sqrt{\ln(2)}$. As the source strengths in the experiments, represented in Fig. 8 as a function of the frequency, and in the numerical simulations, given in the preceding equation, are not the same, the comparisons of the results in the frequency domain are shown for the ratio \hat{p}/S , which does not depend on the source characteristics. For the comparisons in the time domain, the ratio \hat{p}/S determined from the numerical simulations is multiplied by the source strength of the experimental source S_{exp} , and the numerical waveforms are obtained by an inverse Fourier transform of the result.

As the simulations are performed in a two-dimensional geometry, only the projection of the wind vector in the measurement plane is considered. The implemented wind profile is thus

$$\mathbf{V}_0(x, z) = V_0(z - H(x)) \cos \theta_0 \mathbf{e}_x, \quad (14)$$

where the angle relative to the propagation plane has been set to $\theta_0 = 293^\circ$ for both source heights. As $\cos(\theta_0) = 0.39$, downwind conditions occur during the experiments.

At last, it should be noted that the measurements at the three microphones are synchronous in time. However, the time at which each shot was fired is not known. For comparison with the numerical simulation, the time origin is chosen such that the time of arrival of the direct wave is the same at the receiver M_1 ($x = 7.5$ m) for the numerical and experimental results.

The numerical domain is $[-5 \text{ m}; 105 \text{ m}] \times [0 \text{ m}; 15 \text{ m}]$ and has 11 000 points in the ξ -direction and 1501 points in the η -direction. The mesh is uniform with $\Delta\xi = \Delta\eta = 0.01$ m. For frequencies below the limit value of 3 kHz, acoustic waves are discretized with more than ten points per wavelength. Therefore, numerical errors generated by the finite-difference schemes are expected to be negligible. The

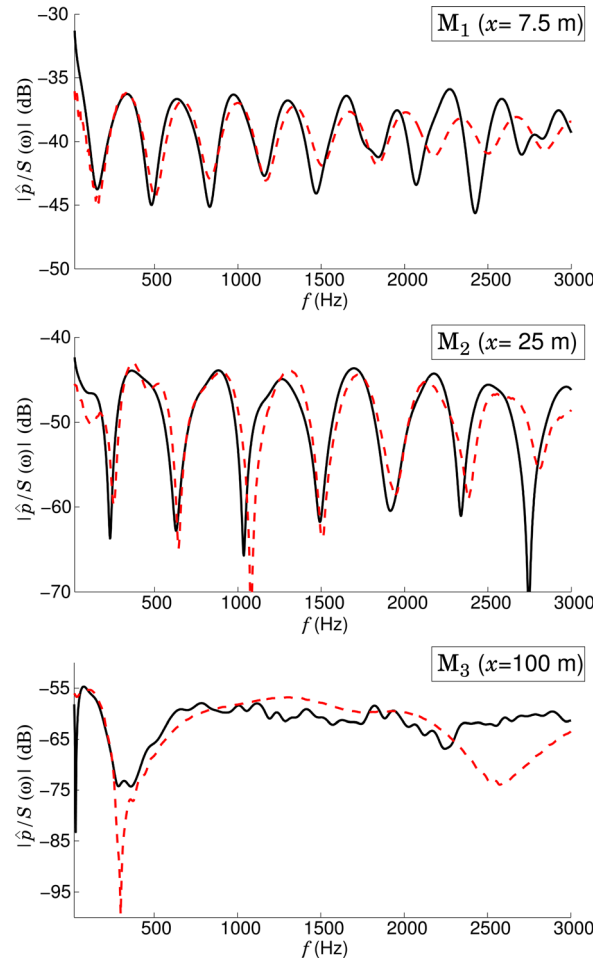


FIG. 11. (Color online) Energy spectral densities normalized by the source strength for a source height of $z_S = 1$ m at the receivers (a) M_1 ($x = 7.5$ m), (b) M_2 ($x = 25$ m), and (c) M_3 ($x = 100$ m) as a function of the frequency: experiment (solid line) and numerical prediction (dashed line). The reference for the dB calculation is 1 m^{-2} .

CFL number, defined by $\text{CFL} = c_0 \Delta t / \Delta \xi$, is set to 0.5. 22 000 time steps are performed. The computation is done on a vector machine NEC SX-8 over 8 CPU hours.

A preliminary simulation using the hard-backed layer impedance model for the ballast surface shows that additional wave arrivals are predicted compared to the measurements. These arrivals are due to the reflection of acoustic waves on the rigid surface below the ballast layer. Two main reasons explain this phenomenon. First, the time-domain boundary condition is derived for locally reacting ground surfaces, which is a valid approximation for most natural grounds. However, as noted in Sec. II B, it is more appropriate to consider extended reaction for ballast surfaces. Second, the impedance model for the ballast has been

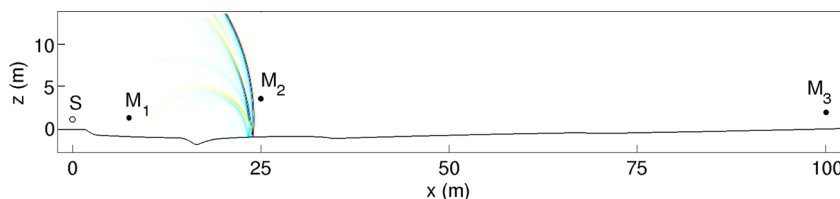


FIG. 10. (Color online) Snapshot of the acoustic pressure at time $t = 71$ ms for the source height $z_S = 1$ m.

TABLE IV. Comparison of the sound exposure levels in dB determined from the experiments and from the numerical simulations. The reference for the dB calculation is $4 \times 10^{-10} \text{ Pa}^2 \text{ s}$.

	$z_S = 1 \text{ m}$			$z_S = 2 \text{ m}$		
	M_1 $x = 7.5 \text{ m}$	M_2 $x = 25 \text{ m}$	M_3 $x = 100 \text{ m}$	M_1 $x = 7.5 \text{ m}$	M_2 $x = 25 \text{ m}$	M_3 $x = 100 \text{ m}$
Experimental result	101.1	92.2	79.3	99.4	90.2	76.7
Numerical prediction	100.5	92.0	79.1	101.5	91.3	78.5

obtained from the measurements performed in the IFSTTAR's site in Bouguenais. As the ballast rocks were put on a rigid ground, the rigidly backed layer model is well adapted to this configuration. However, as the acoustic properties of the layer below the ballast bed in La Veuve site are unknown, it is difficult to extrapolate the use of the rigidly backed layer model to this case. Therefore, the ballast layer is assumed to be infinite in the following section to eliminate these additional arrivals.

B. Comparison of the results

A snapshot of the acoustic pressure at $t = 71 \text{ ms}$ is presented in Fig. 10 for the source height $z_S = 1 \text{ m}$. Three contributions are preponderant in the acoustic field close to the

ground. The first one is the direct wave. The second one is the wave reflected on the soil. At last, the wave diffracted by the gap can be clearly distinguished.

First, results obtained for the case $z_S = 1 \text{ m}$ are considered. The normalized energy spectral densities obtained at the three receivers from the measurements and from the numerical simulation are plotted in Fig. 11 as a function of the frequency. A good agreement is found. Locations of interferences are well predicted over the frequency band of interest, except at the receiver M_1 ($x = 7.5 \text{ m}$) at which some discrepancies can be observed for frequencies higher than 2 kHz .

The sound exposure level:

$$\text{SEL} = 10 \log_{10} \left[\int_{-\infty}^{\infty} \frac{p(t)^2}{P_{\text{ref}}^2} dt \right], \quad (15)$$

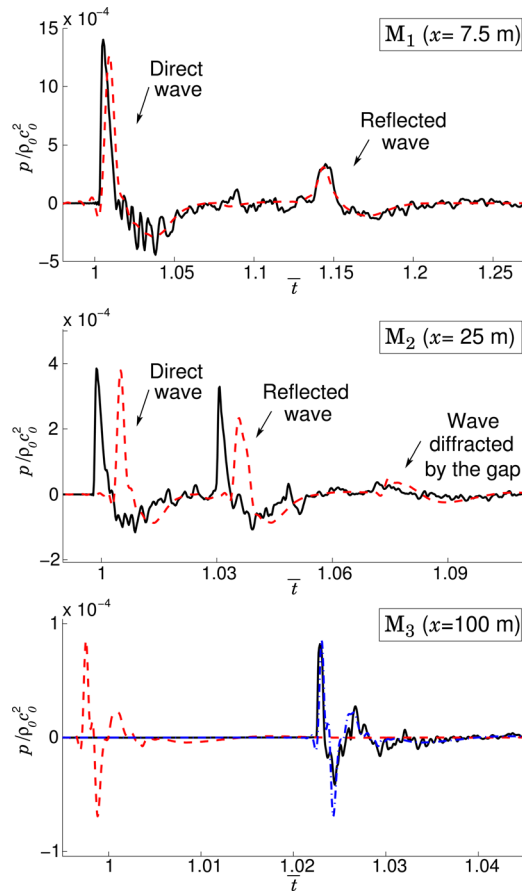


FIG. 12. (Color online) Pressure waveforms as a function of the normalized time $\bar{t} = c_0 t / x$ for a source height of $z_S = 1 \text{ m}$ at the receivers (a) M_1 ($x = 7.5 \text{ m}$), (b) M_2 ($x = 25 \text{ m}$), and (c) M_3 ($x = 100 \text{ m}$): experiment (solid line), numerical prediction (dashed line) and numerical prediction with time-alignment (dash-dotted line).

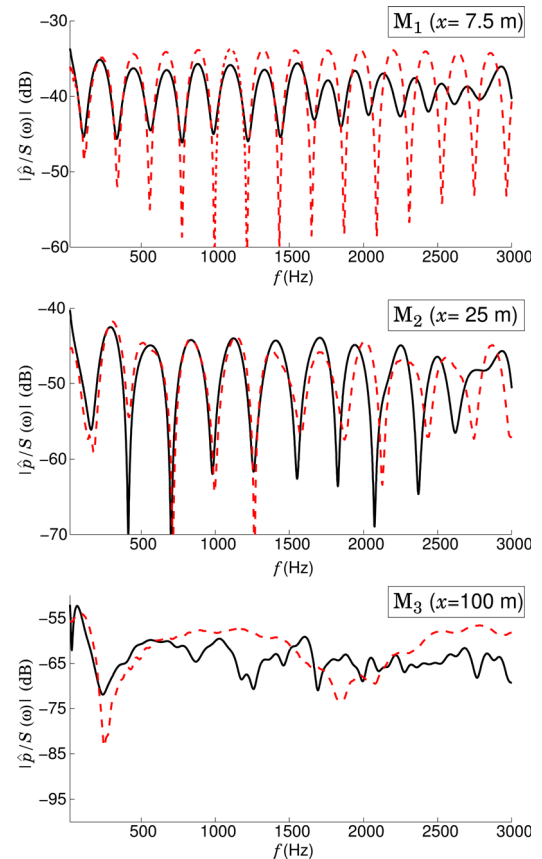


FIG. 13. (Color online) Energy spectral densities normalized by the source strength for a source height of $z_S = 2 \text{ m}$ at the receivers (a) M_1 ($x = 7.5 \text{ m}$), (b) M_2 ($x = 25 \text{ m}$), and (c) M_3 ($x = 100 \text{ m}$) as a function of the frequency: experiment (solid line) and numerical prediction (dashed line). The reference for the dB calculation is 1 m^{-2} .

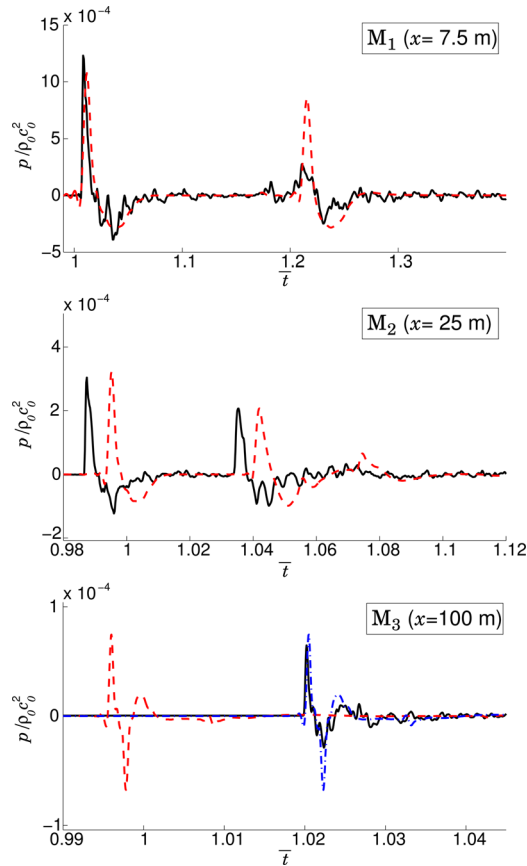


FIG. 14. (Color online) Pressure waveforms as a function of the normalized time $\bar{t} = c_0 t/x$ for a source height of $z_S = 2$ m at the receivers (a) M_1 ($x = 7.5$ m), (b) M_2 ($x = 25$ m), and (c) M_3 ($x = 100$ m): experiment (solid line), numerical prediction (dashed line), and numerical prediction with time-alignment (dash-dotted line).

with $p_{\text{ref}}^2 = 4 \times 10^{-10} \text{ Pa}^2 \text{ s}$, is given in Table IV for the different cases. The largest difference is 0.6 dB for $x = 7.5$ m.

The waveforms are plotted in Fig. 12 as a function of the normalized time $\bar{t} = c_0 t/x$. For the receiver M_1 ($x = 7.5$ m), the waveform obtained from the numerical simulation is similar to the measured one. It can be remarked that the shape of the waveforms corresponding to the reflected wave are in close agreement. At the receiver M_2 ($x = 25$ m), a good matching is obtained. In particular, the arrival at a time $\bar{t} = 1.07$ which corresponds to the wave diffracted by the gap located at $x = 20$ m is retrieved. Nevertheless, a time-shift is observed. It can be linked to an error on the position of the source and/or of the receiver of $\Delta x = c_0 \Delta t = 0.2$ m. The relative error on the time of arrival is less than 1%. At the receiver M_3 , located at $x = 100$ m, the contributions overlap, and it is difficult to distinguish the different waves. In this case, the time-shift is larger. It corresponds to a relative error of 2.5%. The numerical waveform is plotted again in Fig. 12(c) with a modification of the time of arrival to superimpose the waveforms. Despite the time-shift, a good agreement on the shape of the waveforms can be observed.

Comparisons with the experimental data are now presented for a source height of $z_S = 2$ m. Figure 13 shows the energy spectral densities determined from the measurements

and from the numerical results as a function of the frequency. For the receivers M_1 ($x = 7.5$ m) and M_2 ($x = 25$ m), more interference patterns than in Fig. 11 are observed. Good agreement is obtained up to 2 kHz. At the receiver M_3 (100 m), the low frequency part of the signal is well retrieved. An interference is predicted in the numerical results at $f = 1700$ Hz, which is not clearly seen on the measurements. Differences for the SEL are larger than for the case $z_S = 1$ m, with a maximal difference of 2.1 dB.

Waveforms measured and obtained from the numerical simulation for a source height of $z_S = 2$ m are plotted in Fig. 14 as a function of the normalized time $\bar{t} = c_0 t/x$. At the receiver M_1 ($x = 7.5$ m), similarly to the case $z_S = 1$ m, the time delay between the direct and reflected waves is retrieved. A part of the reflected wave is missing in the results of the numerical simulation. At the receivers M_2 ($x = 25$ m) and M_3 ($x = 100$ m), a good matching is obtained with the same time shifts than those observed for the case $z_S = 1$ m.

C. Influence of the wind direction

The influence of the wind direction on the numerical results is briefly discussed. For that, additional simulations are performed for several values of the angle θ_0 for the

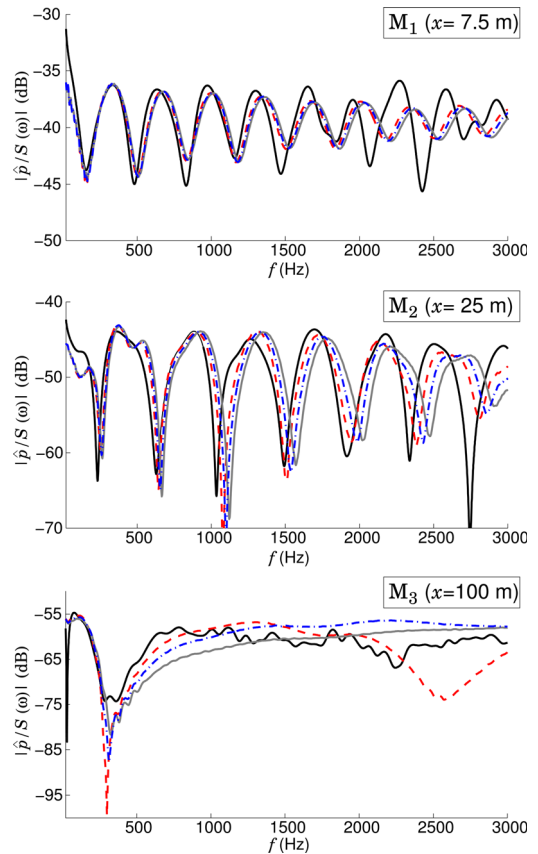


FIG. 15. (Color online) Energy spectral densities normalized by the source strength for a source height of $z_S = 1$ m at the receivers (a) M_1 ($x = 7.5$ m), (b) M_2 ($x = 25$ m), and (c) M_3 ($x = 100$ m) as a function of the frequency: experiment (black solid line) and numerical prediction for $\cos(\theta_0) = -0.39$ (gray solid line), for $\cos(\theta_0) = 0$ (dash-dotted line), and for $\cos(\theta_0) = 0.39$ (dashed line). The reference for the dB calculation is 1 m^{-2} .

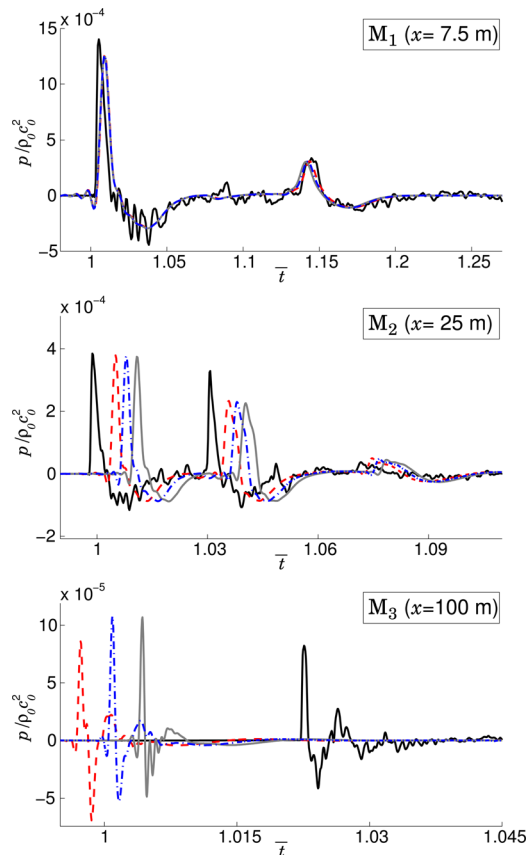


FIG. 16. (Color online) Pressure waveforms as a function of the normalized time $\bar{t} = c_0 t/x$ for a source height of $z_S = 2$ m at the receivers (a) M_1 ($x = 7.5$ m), (b) M_2 ($x = 25$ m), and (c) M_3 ($x = 100$ m): experiment (black solid line) and numerical prediction for $\cos(\theta_0) = -0.39$ (gray solid line), for $\cos(\theta_0) = 0$ (dash-dotted line) and for $\cos(\theta_0) = 0.39$ (dashed line).

source height $z_S = 1$ m. Figure 15 shows the energy spectral densities at the three receivers obtained for the angles $\theta_0 = 67^\circ$, 180° , and 293° , corresponding, respectively, to upwind conditions with $\cos(\theta_0) = -0.39$, no-wind conditions with $\cos(\theta_0) = 0$, and downwind conditions with $\cos(\theta_0) = 0.39$. At the receivers M_1 and M_2 , the effects of the

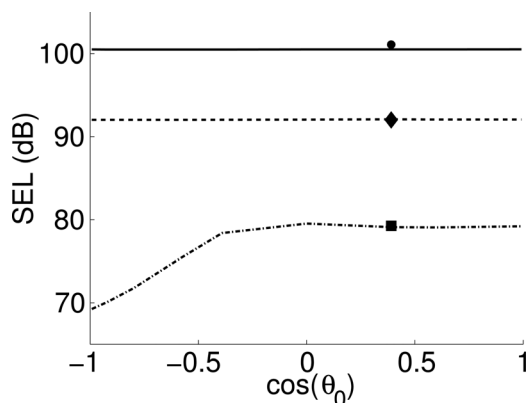


FIG. 17. Sound exposure levels as a function of $\cos(\theta_0)$ computed from the results of the numerical solution at the receivers M_1 (solid line), M_2 (dashed line), and M_3 (dash-dotted line) and from the experimental data at M_1 (circle), M_2 (diamond), and M_3 (square). The reference for the dB calculation is $4 \times 10^{-10} \text{ Pa}^2 \text{ s}$.

meteorological conditions are only visible for frequencies higher than 2 kHz, resulting in a shift of the spectrum toward high frequencies. The spectra at the receiver M_3 are, however, clearly modified. For instance, the value obtained for frequencies around 1 kHz strongly depends on the wind conditions. The dip observed in the preceding section around a frequency of 2.5 kHz does not appear anymore in the frequency band of interest. Only the low frequency content below 300 Hz is left unchanged by varying the wind direction.

Corresponding waveforms are plotted as a function of the time in Fig. 16. All the waveforms are superimposed at the receiver M_1 . At the receiver M_2 , the waveforms have a similar shape, but a time shift due to the differences in propagation time is observed. The waveforms at the receiver M_3 are strongly modified. The minimum and maximum values of the pressure highly depends on the meteorological conditions. Oscillations are also observed on the waveform obtained in upwind conditions [$\cos(\theta_0) = -0.39$] during the expansion phase and are not present in the other two configurations.

The sound exposure levels computed at the three receivers are plotted in Fig. 17 as a function of $\cos(\theta_0)$. At the receivers M_1 ($x = 7.5$ m) and M_2 ($x = 25$ m), the meteorological conditions have only small effects on the SEL, as the curves are almost constant. However, the wind direction has a large impact on the SEL for the receiver M_3 ($x = 100$ m). In particular, for $\cos(\theta_0) < 0$ which corresponds to upwind condition, the SEL is smaller than that obtained from the measurements. A maximal difference of 10 dB is reached for $\cos(\theta_0) = -1$. The variations of the SEL in downwind conditions are smaller, as the SEL has almost the same value for $\cos(\theta_0) > 0$.

IV. CONCLUSION

An experimental campaign carried out on a railway site with a non-flat terrain and a mixed-impedance ground is presented. The main parameters describing the propagation environment are used as input data in a numerical solver of the linearized Euler equations. Acoustic pressure waveforms measured at receivers located on a propagation path are in close agreement with those obtained from the simulation. In the frequency domain, a good correspondence is found for frequencies below 2 kHz. The discrepancies for higher frequencies can be explained by an uncertainty on the position of the source and of the receivers. The study shows that broadband sound propagation over a realistic site with both ground and meteorological effects can be accurately predicted using time-domain approaches.

Future works will focus on the modeling of moving sources for transportation noise applications with time-domain methods. In particular, coupled effects of a moving source and of a complex site on the acoustic pressure field will be studied.

ACKNOWLEDGMENTS

The authors would like to express their gratitude to Sélime Bellaj, Michel Leterrier, and Sylvain Bossier from SNCF test department. Benoit Gauvreau, Philippe L'Hermite, and Rémi

Rouffaud from IFSTTAR are greatly acknowledged for having performed surface impedance measurements. This work was granted access to the HPC resources of IDRIS under the allocation 2011-022203 made by GENCI (Grand Equipement National de Calcul Intensif). It was performed within the framework of the Labex CeLyA of Université de Lyon, operated by the French National Research Agency (Grant No. ANR-10-LABX-0060/ANR-11-IDEX-0007).

Albert, D. G., and Orcutt, J. A. (1990). "Acoustic pulse propagation above grassland and snow: Comparison of theoretical and experimental waveforms," *J. Acoust. Soc. Am.* **87**, 93–100.

ANSI/ASA S1.18-2010 (2010). *Method for Determining the Acoustic Impedance of Ground Surfaces* (American National Standards Institute).

Attenborough, K. (1985). "Acoustical impedance models for outdoor ground surfaces," *J. Sound. Vib.* **99**(4), 521–544.

Attenborough, K., Bashir, I., and Taherzadeh, S. (2011). "Outdoor ground impedance models," *J. Acoust. Soc. Am.* **129**, 2806–2819.

Bass, H. E., Sutherland, L. C., Zuckerwar, A. J., Blackstock, D. T., and Hester, D. M. (1995). "Atmospheric absorption of sound: Further developments," *J. Acoust. Soc. Am.* **97**, 680–683.

Bérenghier, M., Stinson, M. R., Daigle, G. A., and Hamet, J. F. (1997). "Porous road pavement: Acoustical characterization and propagation effects," *J. Acoust. Soc. Am.* **101**, 155–162.

Bogey, C., and Bailly, C. (2004). "A family of low dispersive and low dissipative explicit schemes for flow and noise computations," *J. Comput. Phys.* **194**, 194–214.

Cotté, B. (2008). "Propagation acoustique en milieu extérieur complexe: Problèmes spécifiques au ferroviaire dans le contexte des trains à grande vitesse" ("Outdoor sound propagation in complex environments: Specific problems in the context of high speed trains"), Ph.D. thesis No. 2008-19, École Centrale de Lyon, http://tel.archives-ouvertes.fr/docs/00/66/04/94/PDF/These_Cotte.pdf (Last viewed 4/15/13).

Cotté, B., Blanc-Benon, P., Bogey, C., and Poisson, F. (2009). "Time-domain impedance boundary conditions for simulations of outdoor sound propagation," *AIAA J.* **47**, 2391–2403.

Cramer, O. (1993). "The variation of the specific heat ratio and the speed of sound in air with temperature, pressure, humidity, and CO₂ concentration," *J. Acoust. Soc. Am.* **93**, 2510–2516.

Cramond, A. J., and Don, C. G. (1985). "Impulse propagation over grassland in the presence of temperature and wind gradients," *J. Acoust. Soc. Am.* **78**, 1029–1037.

Dragna, D. (2011). "Modélisation par une approche temporelle de la propagation acoustique en milieu extérieur: Traitement de frontières complexes

et validation sur site ferroviaire" ("Time-domain approach for outdoor sound propagation: Treatment of complex boundaries and validation on a railway site"), Ph.D. thesis No. 2011-35, École Centrale de Lyon, http://tel.archives-ouvertes.fr/docs/00/68/75/19/PDF/TH_T2233_ddragna.pdf (Last viewed 4/15/13).

Dragna, D., Blanc-Benon, P., and Poisson, F. (2013). "Time-domain solver in curvilinear coordinates for outdoor sound propagation over complex terrain," *J. Acoust. Soc. Am.* **133**, 3751–3763.

Dragna, D., Cotté, B., Blanc-Benon, P., and Poisson, F. (2011). "Time-domain simulations of outdoor sound propagation with suitable impedance boundary conditions," *AIAA J.* **49**, 1420–1428.

Guillaume, G., Picaut, J., Dutilleul, G., and Gauvreau, B. (2011). "Time-domain impedance formulation for transmission line matrix modelling of outdoor sound propagation," *J. Sound. Vib.* **330**, 6467–6481.

Heimann, D. (2010). "On the efficiency of noise barriers near sloped terrain—A numerical study," *Acta Acust. Acust.* **96**, 1003–1011.

Heutschi, K. (2009). "Sound propagation over ballast surfaces," *Acta Acust. Acust.* **95**, 1006–1012.

Hornikx, M., Waxler, R., and Forsén, J. (2010). "The extended Fourier pseudospectral time-domain method for atmospheric sound propagation," *J. Acoust. Soc. Am.* **128**, 1632–1646.

Miki, Y. (1990). "Acoustical properties of porous materials—Modifications of Delany-Bazley models," *J. Acoust. Soc. Jpn.* **11**, 19–24.

Ostashev, V. E., Wilson, D. K., Liu, L., Aldridge, D. F., Symons, N. P., and Marlin, D. (2005). "Equations for finite-difference, time-domain simulation of sound propagation in moving inhomogeneous media and numerical implementation," *J. Acoust. Soc. Am.* **117**, 503–517.

Parakkal, S., Gilbert, K. E., Di, X., and Bass, H. E. (2010). "A generalized polar coordinate method for sound propagation over large-scale irregular terrain," *J. Acoust. Soc. Am.* **128**, 2573–2580.

Rasmussen, K. B. (1981). "Sound propagation over grass covered ground," *J. Sound. Vib.* **78**(2), 247–255.

Salomons, E. (2001). *Computational Atmospheric Acoustics* (Kluwer Academic Publishers, Dordrecht), pp. 117–118 and 279–287.

Salomons, E. M., Blumrich, R., and Heimann, D. (2002). "Eulerian time-domain model for sound propagation over a finite-impedance ground surface. Comparison with frequency-domain models," *Acta Acust. Acust.* **88**, 483–492.

Tam, C. K. W., and Dong, Z. (1996). "Radiation and outflow boundary conditions for direct computation of acoustic and flow disturbances in a non-uniform mean flow," *J. Comput. Acoust.* **4**, 175–201.

Van Renterghem, T., and Botteldooren, D. (2003). "Numerical simulation of the effect of trees on downwind noise barrier performance," *Acta Acust. Acust.* **89**, 764–778.

Wilson, D. K., Ostashev, V. E., Collier, S. L., Symons, N. P., Aldridge, D. F., and Marlin, D. H. (2007). "Time-domain calculations of sound interactions with outdoor ground surfaces," *Appl. Acoust.* **68**, 173–200.